3D Transcranial Ultrasound Localization Microscopy in the Rat Brain With a Multiplexed Matrix Probe

Arthur Chavignon, Baptiste Heiles, Vincent Hingot, Cyrille Orset, Denis Vivien, Olivier Couture

3D Transcranial Ultrasound Localization Microscopy in the Rat Brain with a Multiplexed Matrix Probe

Arthur Chavignon, Baptiste Heiles, Vincent Hingot, Cyrille Orset, Denis Vivien, Olivier Couture

***Abstract*— *Objective:* Ultrasound Localization Microscopy (ULM) provides images of the microcirculation in-depth in living tissue. However, its implementation in two-dimension is limited by the elevation projection and tedious plane-by-plane acquisition. Volumetric ULM alleviates these issues and can map the vasculature of entire organs in one acquisition with isotropic resolution. However, its optimal implementation requires many independent acquisition channels, leading to complex custom hardware. *Methods:* In this article, we implemented volumetric ultrasound imaging with a multiplexed 32 × 32 probe driven by a single commercial ultrasound scanner. We propose and compare three different sub-aperture multiplexing combinations for localization microscopy in silico and in vitro with a flow of microbubbles in a canal. Finally, we evaluate the approach for micro-angiography of the rat brain. The "light" combination allows a higher maximal volume rate than the "full" combination while maintaining the field of view and resolution. *Results*: In the rat brain, 100,000 volumes were acquired within 7 min with a dedicated ultrasound sequence and revealed vessels down to 31 µm in diameter with flows from 4.3 mm/s to 28.4 mm/s. *Conclusion:* This work demonstrates the ability to perform a complete angiography with unprecedented resolution in the living rat's brain with a simple and light setup through the intact skull. *Significance:* We foresee that it might contribute to democratize 3D ULM for both preclinical and clinical studies.**

***Index Terms*— Brain microvascularization, multiplexed probe, super-resolution ultrasound, transcranial ultrasound imaging, 3D ultrasound localization microscopy.**

I. Introduction:

The brain microvascular system is a complex mesh of capillaries (<10 µm diameter) linked to wider arterioles and venules ([25-150] µm diameter) that feed neurons with glucose and oxygen. Modifications of blood flow and tissue perfusion are directly related to neural activity [1]. Malfunctions of this vascular network are involved in several disease processes, and visual analyses are necessary for diagnosis. However, imaging at microscopic scales with a deep penetration remains a challenge for *in vivo* imaging techniques.

Some *ex vivo* techniques reach resolutions of a few microns, such as micro angio-computed tomography [2], [3]. Tissue optical clearing approaches offer an alternative with either microscopic resolution for vascular imaging (DISCO) [4], [5], nervous system (CLARITY) [6], [7], and fluorescent proteins imaging (CUBIC) [8]. For blood flow dynamics, 2-photons intravital microscopy provides arterioles and venules vasodynamic with an almost one-millimeter depth of imaging in the pia mater of the rat brain with craniectomy [9].

Ultrasound Localization Microscopy (ULM) is becoming an attractive option for *in vivo* microvascularization imaging [10]–[12]. By imaging isolated microbubbles with a sub-wavelength precision and tracking their propagation in blood vessels, it reveals the microvascularization of organs in small animals *in vivo* with a resolution of tens of microns: brain through a thinned skull [13] or with craniectomy [14], ear [15], kidney [16], [17], and other [18]–[22], and recently in the human kidney, liver, pancreas, breast, and brain [23], [24].

However, 2D ULM suffers elevation projection of the probe. It hinders imaging transversal vessels and underestimates velocity measurement of microbubbles' flows not aligned in the imaging plane. Moreover, out-of-plane motions cannot be tracked and corrected for moving organs. The necessity for careful selection of the imaging plane also induces a very high user dependency and a tedious approach to explore entire organs. Volumetric imaging becomes essential to solve these drawbacks.

For appropriate microbubble tracking in three-dimensional ULM, volume rates of hundreds of frames per second would be favorable. Unfortunately, conventional 3D ultrasound scanners use time-consuming line-by-line or sector-by-sector scanning techniques with a limit of a few tens of volumes per second. Recent developments in ultrafast imaging [25], [26] opened the possibility for a high-volume rate 3D ultrasound. The most straightforward implementation of volumetric ultrafast imaging consists of a numerous 2D matrix array where each element is connected to an independent channel of an ultrasound scanner [27]. For a matrix with 1024 transducers (32 × 32), 4 ultrasounds scanners of 256 channels each must be synchronized to control the entire probe [27]–[31]. New perspectives to reduce the number of channels are brought about by new ultrasound research scanners, high flexibility in ultrasound sequence programming, and customized probes and electronics. Sparse arrays use a fraction of transducers in a

This study was funded by the European Research Council within the H2020 program (ERC Cog ResolveStroke 772786).
A. Chavignon, V. Hingot, O. Couture are with Sorbonne Université, CNRS, INSERM, Department Laboratoire d'Imagerie Biomedicale, Paris, France. (arthur.chavignon.pro@gmail.com, vincent.hingot@sorbonne-universite.fr, olivier.couture@sorbonne-universite.fr)
B. Heiles is with Maresca Lab, TU Delft, Netherlands. (baptiste.heiles@gmail.com)
C. Orset and D. Vivien are with Normandie Univ, UNICAEN, INSERM U1237, Etablissement Français du Sang, Physiopathology and Imaging of Neurological Disorders (PhIND), Cyceron, Institut Blood and Brain @ Caen-Normandie (BB@C), Caen, France. D. Vivien is also with Department of clinical research, Caen-Normandie University Hospital, CHU, Avenue de la côte de Nacre, Caen, France. (orset@cyceron.fr, vivien@cyceron.fr).

matrix array to perform volumetric imaging [32]–[34]. Row-column addressed (RCA) matrix probes exploited the orthogonal properties of two linear arrays to get an isotropic resolution on a large field of view [35]–[37]. However, these two last approaches pay the reduction of the channel by decreasing the imaging capability. Multiplexing systems try to preserve the imaging quality but require more transmission, affecting the maximal volume rate system [32], [38], [39]. ULM has already been implemented in 3D with encouraging results *in vitro* [40], [41], with sparse matrix array [33], with RCA matrix probes [42], particularly with synchronized ultrasounds scanners [43]. This last system was used *in vivo* to image the rat brain with craniectomy [44].

In this article, we implemented ultrafast volumetric imaging on a research scanner with a multiplexed matrix probe and performed 3D ULM *in vivo* in the rat brain with an intact skull. The 1024 transducers of the probe were divided into four sub-apertures controlled by one commercial ultrasound scanner with 256 channels. Pulse transmissions were sent by one sub-aperture, and backscattered echoes were received by another sub-aperture. Therefore, to reach the fully addressed array imaging capability, 16 couples of transmission-reception were required (4 transmissions × 4 receptions). In this study, we defined and evaluated two multiplexing combinations, "direct" and "light", with fewer transmission-reception couples. The "light" combination preserved the imaging capability of a fully addressed array and allowed an imaging volume rate compatible with *in vivo* imaging of the brain micro-vascularization. The dedicated ultrasound sequence limited the amount of generated data and enabled long acquisition without volume number limitations. We compared imaging qualities of the 3 different multiplexing combinations *in silico* with point spread function simulation and *in vitro* with a microbubbles flow in a tube. Finally, the "light" combination was applied for *in vivo* experiments on a rat brain with an intact skull revealing the microcirculation.

II. Methods:

A. *Optimized volumetric imaging with a multiplexed matrix probe*

Ultrafast volumetric imaging was performed with a single Vantage 256™ Research Ultrasound Systems (Verasonics, Inc., Kirkland, WA, USA) driving a matrix probe of 1024 elements (central frequency 7.8 MHz, 56 % bandwidth at -6 dB) (Vermon, Tours, France) via the Verasonics UTA 1024-MUX adapter. Transducers were aligned on a 35 × 32 grid with a 300 µm pitch. Rows 9, 17, and 25 were unpopulated, yielding a 9.6 mm × 10.5 mm field-of-view (Fig. 1(a)). Each sampling channel was wired to one of the 256 switches of the MUX adapter and could be connected successively to one transducer among 4: channel i can be connected to transducers i, i+256, i+512, or i+712 (Fig. 1(a)), with a commutation time of 4 µs approximatively (constructor datasheet). It enabled changing switches' states between the transmission of a pulse and the reception of its echoes. We defined 4 sub-apertures composed of 256 successive channels, starting from channels 1, 257, 513, and 769. These sub-apertures corresponded to the four active layer panels of 32 × 8 transducers assembled to get the wide matrix array. The relative positions of active layer panels were

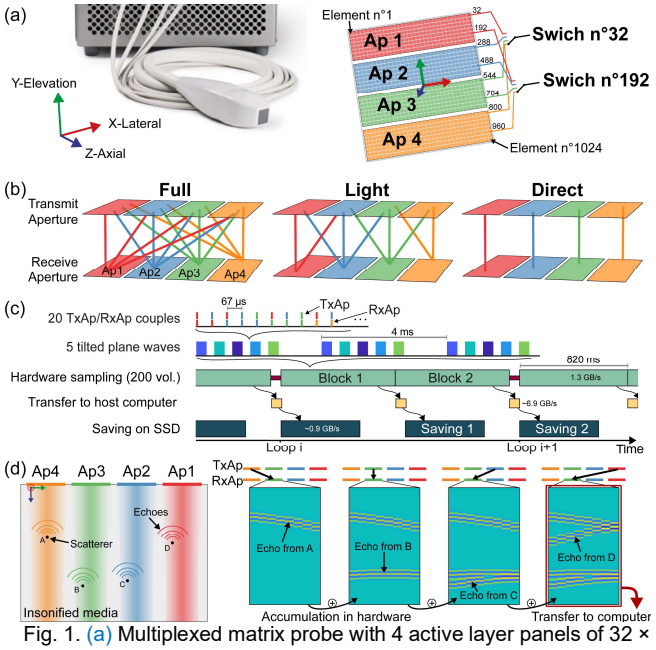

Fig. 1. (a) Multiplexed matrix probe with 4 active layer panels of 32 × 8 transducers elements, divided into 4 sub-apertures. The 256 switches of the 1-4 MUX can address 1 transducer among 4. (b) "Direct", "full" and "light" multiplexing combinations. Links represent the transmission aperture/reception aperture (TxAp/RxAp) couples. (c) Timeline of the asynchronous sequence. Each block of 200 volumes was composed of a set of 5 plane waves requiring each 10 TxAp/RxAp couples. (d) Echoes generated by successive transmit apertures (TxAp) and received by aperture 2 (RxAp) were accumulated directly in hardware before being transferred to the host computer.

calibrated to correct offsets and angulations. We measured a maximal offset of 145 µm (0.73 λ) in the lateral direction, and an angulation of 2.1° (lateral axis) between two panels, yielding a maximal axial offset of 114 µm (0.58 λ) between transducers.

Each transmission of a plane wave requires multiple pulse emissions with different apertures of 256 transducers in transmission and reception to recover echoes from all scatterers with any transducer. Transmission Aperture/Reception Aperture (TxAp/RxAp) defines a couple of apertures used for emission and reception of one pulse emission. The high versatility of this system allows us to mix the apertures to reduce the number of pulses needed to reconstruct one full volume with a good quality Point Spread Function (PSF).

We defined three different multiplexing combinations: lists of TxAp/RxAp couples used to sample one plane wave (Fig. 1(b)).

1. The "full" combination: equivalent to a fully addressed matrix array, each aperture received echoes provided by the emission of each aperture, leading to 16 couples TxAp/RxAp per plane wave.
2. The "direct" combination: equivalent to 4 individual 32 × 8 matrix probes, each aperture received the echoes generated by itself, leading to only 4 couples per plane wave.
3. The "light" combination: each aperture received the echoes generated by itself and its first neighbor's apertures, leading to 10 couples per plane wave. For example, aperture 2 acquired the echoes generated by apertures 1, 2, and 3.

The combination will limit the maximal volume rate of imaging. For *in vivo* acquisition, the maximal acquisition depth was fixed at 16.4 mm, with a pulse repetition frequency (PRF) of 15 kHz. This value was set lower than the maximal PRF (40

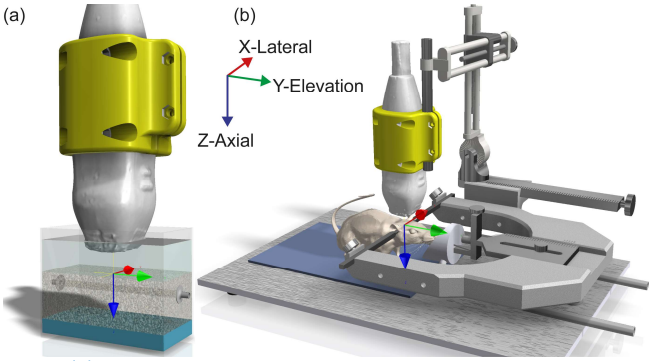

Fig. 2. (a) *In vitro* setup with a 0.5 mm diameter tube molded in agar, oriented in the elevation direction of the probe (y-axis). The bottom of the tank was covered with an acoustic absorber and water was used to fill the gap between the agar and the probe. (b) *In vivo* setup of the rat brain imaging with a stereotaxic frame constraining rat's head, and holding the matrix probe. The rat was anesthetized with isoflurane via an inhalation mask, and its temperature was regulated with a heating pad. Sonovue microbubbles were injected with a tail vein catheter.

kHz) to prevent hardware lags. Volumes were obtained by compounding 5 bidimensional plane waves after Delay-And-Sum beamforming. Tilting angles were (Azimuth, Elevation): {(0, 0); (-5, 0); (5, 0); (0, -5); (0, 5)} in degrees. The maximal compounded volume rate (CVR) was devised from the PRF, the number of plane waves (N_{PW}) and the number of TxAp/RxAp couples of the multiplexing combination (N_{MUX}): $CVR_{max} = PRF/N_{pw}/N_{MUX}$. For the "direct" combination, the CVR_{max} was 750 Hz, 300 Hz for "light", and 187 Hz for "full".

The 7.8 MHz excitation pulse parameters are exposed in Table 1. with measured peak negative pressure (PNP) and peak positive pressure (PPP) in water. No microbubble disruption was observed *in vitro* in those settings. For transcranial *in vivo* imaging, the skull attenuation calibration attested a reduction of both PNP and PPP by a factor 2 minimum, ensuring no microbubbles destruction inside the rat brain. A maximum thermal elevation of 1°C was measured on the surface of the probe emitting in an acoustic gel.

Echoes were sampled at 31.2 MHz. For quadrature demodulation, only the two first samples out of 4 per period were kept and transferred to the host controller to get the in-phase and quadrature signals with the "NS100BW" mode in Verasonics.

B. *In silico, in vitro, and in vivo validation setups*

We have validated these three different combinations in three different setups:

	In vitro	*In vivo* transcranial
Tension [volt]	10	16
Number of half cycles	2	4
Duty cycle	67 %	67 %
Peak Positive Pressure [kPa]	345	617
Peak Negative Pressure [kPa]	298	662

Table 1. Pulse excitations parameters. The transmission frequency was set in both cases to 7.8 MHz.

1) In silico: Point Spread Function simulation

The 3D PSF of isolated punctual scatterers was simulated with the Verasonics Research Ultrasound Simulator (Verasonics, Inc., Kirkland, WA, USA) with a pulse-echo model. Scatterers were placed in front of sub-aperture 3 (intra-aperture zone), at coordinates [x = -1.35 mm; y = 0], and in the interleaving space between sub-apertures 1 and 2 (inter-aperture zone) at [x = 2.70 mm; y = 0]. Scatterers were imaged at five different depths between z = 1.8 mm (9 λ) to z = 25.2 mm (128 λ).

2) In vitro: microbubbles flow imaging in a canal

A solution of microbubbles (Sonovue, Bracco, Italy) was diluted with a ratio of 1/8000 (between 13 to 63 thousand microbubbles per ml after dilution [45]) and injected in a 0.5 mm wide flow canal embedded downward in agar [43] at a flow rate of 0.50 ml/min (mean velocity 42 mm/s), in the elevation direction (y-axis) (Fig. 2(a)). Radiofrequency data (RF data) generated by each TxAp/RxAp couple were saved independently. All multiplexing combinations were reconstructed in post-processing by selecting the right list of TxAp/RxAp couples to get either "direct", "light" or "full" modes. The CVR was reduced to 200 Hz for deeper imaging up to 125 wavelengths. 20 blocks of 200 continuous volumes were acquired.

3) In vivo feasibility of 3D ULM: transcranial rat brain imaging

All animals' experiments were performed under the European Community Council guidelines (2010/63/EU) and approved by the protocol APAFIS #22544 validated by the French ethics committee "Comité d'éthique Normandie en matière d'expérimentation animale". 5 Sprague-Dawley 6-7 weeks old male rats were placed in a small animal stereotaxic frame (David Kopf stereotaxic instrument, Tujunga, CA, USA) equipped with an anesthesia mask with a mix of isoflurane (2 %) and nitrous oxide (Fig. 2(b)). Ear bars and an incisor bar were used to restrain head motion. The animal's temperature was regulated at 38°C with a heating pad and a rectal probe. The top of the head was shaved and covered with echographic gel. For a few animals, the head skin was scalped to image directly on the skull bone to prevent air bubbles stuck in the remaining hairs and sutured after the imaging sequence. The position of the ultrasonic probe was adjusted using the stereotaxic electrode manipulator (0.1 mm resolution, David Kopf stereotaxic instrument, Tujunga, CA, USA) with a custom 3D printed probe holder. During the 7 minutes of imaging, 14 boluses of 50 µl (every 30 seconds) of Sonovue microbubbles were injected in a tail vein catheter to ensure a constant concentration of microbubbles in the rat blood volume. Two magnets (one inside the syringe, one outside) were softly agitated to prevent aggregations of microbubbles in the solution. 100,000 volumes were acquired in blocks of 200 continuous volumes at 243 Hz CVR, for a total datasize of 245 GB.

C. *Dedicated imaging sequence for volumetric ULM*

The multiplexing setup described in the previous section was used to perform volumetric ULM. A specific asynchronous acquisition sequence was designed and implemented through hardware and software levers to reduce data and acquisition time further.

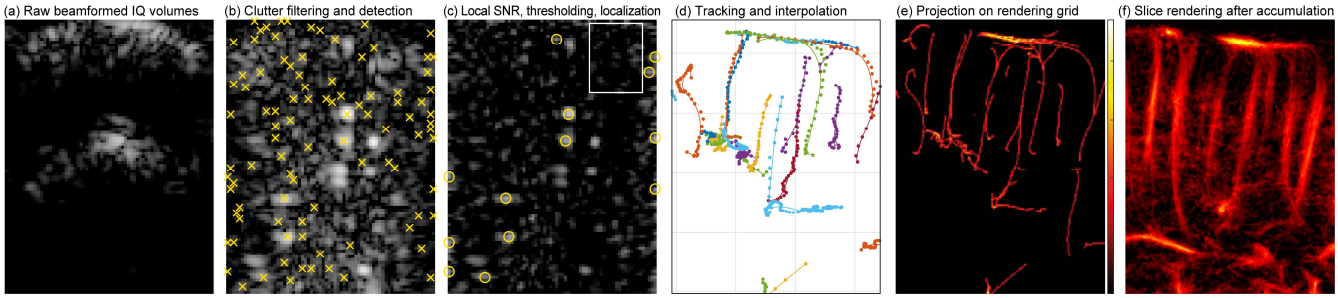

Fig. 3. ULM processing steps. (a) Radiofrequency data were beamformed with a Delay-And-Sum algorithm. (b) IQ volumes were filtered to remove tissue signals, and local maxima were detected (yellow crosses). (c) Maxima with low local SNR were rejected. The remaining maxima were localized with a radial symmetry-based algorithm (only microbubbles centered the slice are surrounded with yellow circles). (d) Microbubbles were paired with a tracking algorithm. Trajectories were interpolated and smoothed. (e) Interpolated trajectories were projected on a rendering volume by counting the occurrence per voxel. (f) After accumulating a large number of trajectories, a power-law compression was applied to the final volume for visual analysis (1/3 or 1/2).

Continuous blocks of 200 volumes were acquired digitalized by the hardware, transferred to the host computer (Intel Core i9 @2.9 GHz 12 cores, 128 GB RAM @2133 MHz) running with MATLAB (The MathWorks Inc., release 2019b, MA, USA) via a PCI-express interface (6.9 GB/s constructor datasheet) (Fig. 1(c)). Data were saved on an SSD (970 PRO 1 To SSD - PCIe 3.0×4 NVMe, Samsung, South Korea) with an estimated writing speed of 900 MB/s ($WriteSpeed$). As soon as the RF data have been transferred to the host computer, a new acquisition of 200 volumes can start without the termination of the saving process (Fig. 1(c)). The sequence was only paused to wait for the saving process between blocs of 200 volumes.

For each transmission, the signal was sampled from 3.7 mm to 16.3 mm from the probe to avoid near-field imaging and reduce data size. For one tilted plane wave, all RF data generated by any transmitting aperture and received by the same aperture were coherently summed in the hardware system's storage memory by using the accumulation mode provided in Verasonics Sequencing software (Fig. 1(d)), reducing the size of the data needed to be transferred and saved. The delay law at emission must be calculated considering the entire grid of 1024 elements. Each tilted plane wave generated 4 buffers of 256 samples ($N_{samples}$) per 256 channels (2.56 MB with 16 bits encoding) whatever the multiplexing combination used thanks to the coherent summation.

We defined a writing volume rate (WVR) to estimate the number of volumes saved on disk per second (considering raw RF data for one volume). In that configuration, the writing volume rate was 343 volumes/s.

$$WVR = \frac{WriteSpeed}{N_{samples} \cdot 256 \cdot 4 \cdot N_{PW} \cdot 2bytes}$$

Under these imaging conditions, the WVR was lower than the CVR, leading to continuous acquisition at 243 Hz.

D. *Volumetric ULM post-processing for hemodynamic angiography*

The general process of ULM was described previously in [12], [43]. RF data was beamformed *a posteriori* with Delay-And-Sum algorithm on CUDA cores (20 ms/volume with NVidia GeForce RTX 2080Ti, RAM 11 GB). Volumes were composed of 70 × 76 × 118 voxels of 150 µm in lateral and elevation direction and 99 µm in the axial direction.

Continuous volumes were filtered with a Singular Value Decomposition filter (SVD) to separate microbubbles from tissue and blood signals (Fig. 3(a-b)) [13], [46]–[48] (12 values removed *in vivo*, 15 *in vitro* over 200 volumes). A local maxima detection function was applied to detect potential microbubbles (yellow crosses on Fig. 3(b)). A local signal-to-noise ratio (SNR) was assigned to each local maximum by comparing the intensity of the local maximum voxel with the local average intensity in a 5 voxels width cube (Fig. 3(c)). Microbubbles with an SNR lower than 9 dB were rejected.

A custom 3D radial symmetry-based localization kernel [44], [49] was implemented to localize the sub-wavelength position of the microbubble, adapted from a 2D scheme [50], [51], avoiding time and space-consuming interpolation schemes. Positions were paired into trajectories with a tracking algorithm based on the Kuhn-Munkres algorithm (Fig. 3(d)) (*simpletracker*, Jean-Yves Tinevez). We fixed a maximal linking distance between two points of 0.3 mm, corresponding to a maximal microbubble's velocity of 73 mm/s and a minimal persistence of 37 ms. Final trajectories were smoothed with a moving average method over 5 points and interpolated with a linear model (Fig. 3(d)) over each dimension to get a maximal distance of 9.8 µm between two samples of a trajectory. A 3D velocity vector was assigned to each point of the oversampled trajectory.

This process ran in 3 hours for *in vivo* imaging on asynchronous workers with MATLAB Parallel Computing Toolbox (The MathWorks Inc., release 2019a, MA, USA) for the 100,000 volumes acquired to generate one ULM volume (corresponding to 245 GB of raw RF data).

E. *3D renderings and hemodynamic measurements*

Two types of rendering were processed with isotropic voxels of 9.8 µm. An Intensity-based volume was built by counting all interpolated trajectories crossing each voxel (Fig. 3(e-f)). A vector flow volume $\overrightarrow{V_{x,y,z}}$ was constructed by averaging velocity vectors of all trajectories crossing each voxel. 3D renderings were performed after a power-law compression (between 1/2 and 1/3 according to rendering mode) with Amira software (ThermoFisher) using the *Volume Rendering* module and maximum (MIP) or alpha compositions.

For the hemodynamic investigation, the volume rendering was performed with the velocity magnitude and color-encoded

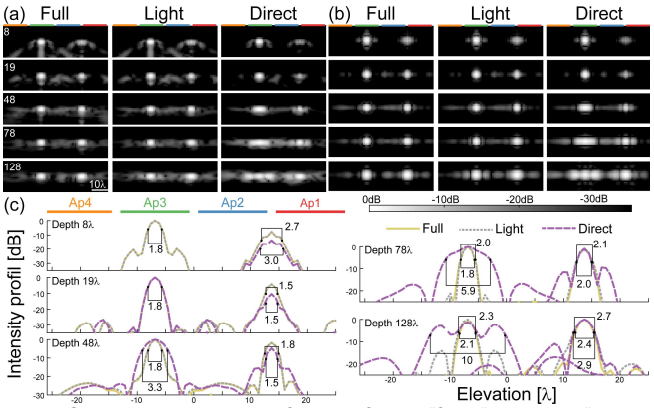

Fig. 4. Simulated point spread function for the "full", "light", and "direct" combinations at different: lateral slices (y-axis) (a) and axial slices (z-axis) (b). (c) Elevation profiles of PSF for all combinations at various depths. The elevation resolution was measured at -6 dB from the central lobe. (λ = 197 µm)

with the axial direction of flux: $norm(\overrightarrow{V_{x,y,z}}) \cdot sign(\overrightarrow{V_{x,y,z}}.\overrightarrow{u_z})$ (with $\overrightarrow{u_z}$ the axial unitary vector).

Vessels' diameters were measured from the hemodynamic volume. The velocity volume was averaged along the centerline of the vessel to build a cross-section velocity map. The section area was obtained by counting the number of pixels with a velocity exceeding half of the maximal velocity of the section and extended to a theoretical pipe section S_0 with a Poiseuille law laminar flow: $S_{v>\frac{1}{2}v_{max}} = \frac{1}{2}S_0$. Finally, the area was converted into an equivalent vessel radius R_{max}. For each vessel, the integral intensity inside the R_{max} was compared to the integral intensity I outside this radius r. This intensity ratio $IR_{I/O}$ gave an indicator of the validity of the radius estimation with the hemodynamic volume. Only measurements with a ratio higher than 70 % were kept.

$$IR_{I/O} = \frac{\int_{r<R_{max}} I(r)}{\int_{R_{max}<r<2.R_{max}} I(r)}$$

To further validate the resolution of our approach, the Fourier Shell Correlation (FSC) [52], [53] was computed. It provides a non-local estimation of the resolution by calculating the correlation of spatial frequencies. The list of microbubble trajectories was split into two sub-population (odd and even indices) used to reconstruct two observations of the same volume. The 2-sigma threshold [52], [54], [55] was applied to get a spatial frequency resolution compared to an expected theoretical pure-noise. The 2-sigma curve is obtained with the number of voxels $n(R)$ in each correlation shell of spatial frequency $1/R$.

$$\sigma(R) = \frac{2}{\sqrt{n(R)/2}}$$

Below this threshold, spatial frequencies are not considered consistent.

F. *Microangio Computed Tomography with µAngiofil perfusion*

After the 3D ULM acquisition, the animal was perfused with µAngiofil (Fumedica AG, Switzerland) according to a published procedure [2]. The animal was heparinized, and internal carotid arteries were cannulated. The brain was widely

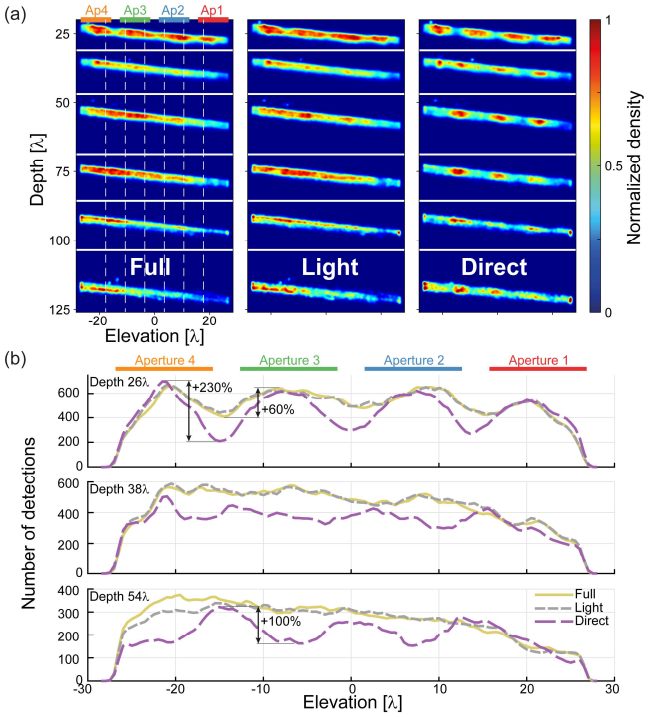

Fig. 5. (a) Localization heatmaps with lateral projection (x-axis) for different combinations. Each canal was processed independently. The figure presents the results normalized on a single image. The white dot lines delineate the inter-aperture zones from the intra-aperture zones. (b) Number of localizations in canal's axis at 26, 38, and 54 wavelengths from the probe (5.1; 7.5; 10.6 mm). (λ = 197 µm)

washed out from blood with saline via catheters. Later, the solution of µAngiofil was perfused in the brain until a complete filling of the vascularization. After polymerization, the head was taken off the animal and fixed in paraformaldehyde. The day after, the brain was extracted from the skull and scanned with a high-resolution micro-CT (micro-Computed Tomography) Skyscan 1172 (Bruker microCT, Kontich, Belgium) with 10 µm voxel size.

III. Results

A. *PSF optimization with sub-aperture management*

The PSF was simulated as a first step to characterize the imaging system. For each combination of transmitting and receiving apertures, main lateral and axial slices are displayed in Fig. 4(a-b). The main elevation profiles are plotted in Fig. 4(c), with the elevation resolution measured at -6 dB. In near-field imaging, all combinations provided approximately the same elevation resolution but with variation between the inter-aperture zone (1.8 λ) and the intra-aperture zone (2.7 λ). PSF intensity was 10 dB lower in the inter-aperture zone with the "light" and "full" combination. In the mid-field imaging (from 19 λ to 78 λ), the "light" and "full" combinations provided a constant resolution of 1.8 λ. The maximal intensity of the PSF was also constant and homogenous. The "direct" combination presented a decreased resolution down to 5.9 λ. Deeper, only the "full" combination managed to keep a constant a good resolution thanks to its wider reception aperture, particularly with the second neighbors TxAp/RxAp couples (e.g. TxAp = 2, RxAp = 4).

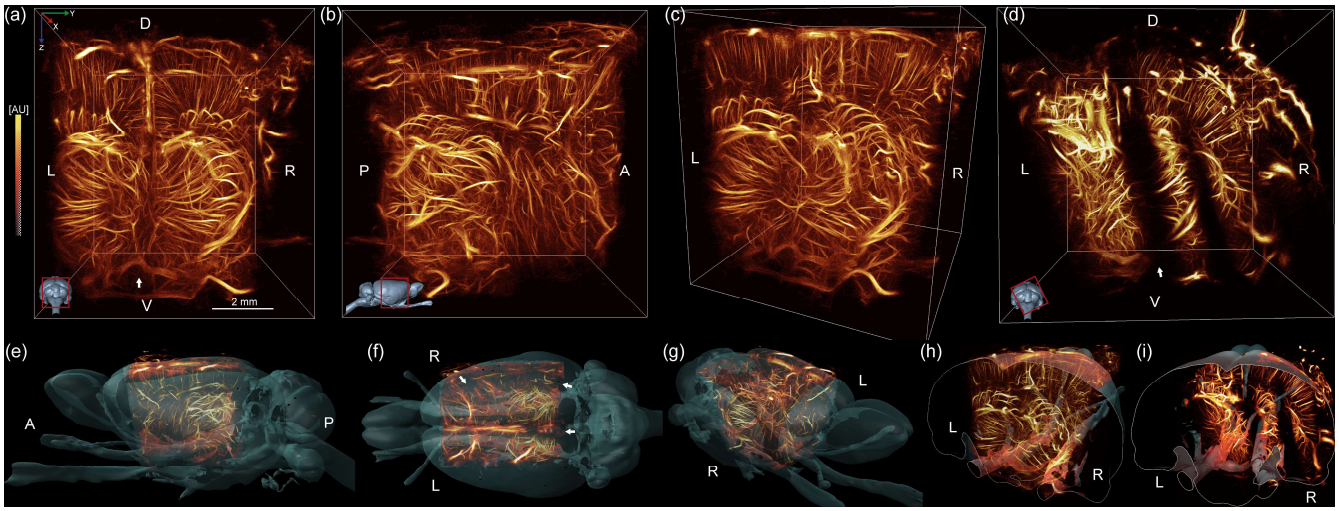

Fig. 6. (a-b-c) 3D rendering MIP of the brain microvascular with Amira (ThermoFisher) : (a) coronal view, (b) sagittal view. Intensity reflects the count of microbubbles. (d) 3D rendering with tilted ultrasound probe on another rat to observe the cortex in the right hemisphere. The shadowed region is now tilted, revealing microvasculature under the sagittal suture. (e-f-g-h-i) 3DULM rendering overlapped with the Waxholm Space Atlas of the Sprague Dawley rat brain, in shaded blue. (i) 3D ULM rendering with a tilted probe. L: left, R: right, A: anterior, P: posterior, D: dorsal, V: ventral. (Power-law compression: 1/2, See supplementary video 1)

B. *Homogenous microbubbles localization within a canal*

We further investigated the characteristics of the different combinations by imaging the *in vitro* phantom with ULM.

Fig. 5(a) shows the distribution of microbubble's localizations at each depth, with a lateral projection (x-axis). The 6 acquisitions of the same pipe with different depths have been summed on the same image. The number of detected microbubbles within the canals is plotted in Fig. 5(b).

The localization density map with a "direct" combination presented a large axial variability with a maximal increase of +230 % between aperture 4 and its right side closed to the probe (Fig. 5(b)). In the near-field, scatterers in inter-aperture zones did not receive enough signal to be imaged correctly, yielding four outlying localization areas. Deeper, when scatterers were located in an inter-aperture zone, the reception area was sheared with two reception aperture and wider than for scatterers facing a sub-aperture. Localizations appeared mostly in the three interleaving zones with a difference of +100 % (aperture 3 and its left side in Fig. 5(a)). The localization density remained homogenous for the "full" and "light" combinations starting from 30 wavelengths (5.9 mm). In the near-field, same as with the "direct" combination, a difference of +60 % occurred between intra-aperture zones and inter-aperture zones. The 6 additional TxAp/RxAp couples of the "full" combination did not improve the number of localizations compared to the "light" combination.

C. *Transcranial volumetric ULM of a rat brain in vivo with an intact skull*

Finally, we imaged a rat brain *in vivo* with an intact skull using the "light" TxAp/RxAp combination within 7 min. 42 M positions of microbubbles were localized, tracked into 541 k trajectories, and binned into 3D intensity volumes exposed in Fig. 6 with a surface mesh of the brain provided by the Waxholm Rat Atlas [56]. It revealed the complex vascular system of the brain from the neocortex to the circle of Willis. Because skull heterogeneities affect the propagation of ultrasound waves, some regions appeared shadowed in the axial direction of the probe, under the sagittal suture on Fig. 6(a) and (d) (white arrows) with an axial shadowed zone. The same aberration appeared under coronal, lambdoidal sutures and temporal crests (white arrows on Fig. 6(f)). The brain's right hemisphere could be recovered by tilting the probe (15° around the y-axis) to bypass the lateral crest (Fig. 6(d)).

Fig. 7(a) shows a volumetric hemodynamic rendering of the brain. The color encoding of upward/downward (red/blue) flow facilitated the visualization of micro-vessels organization in the neocortex on a 600 µm thin slice (Fig. 7(b)). Microbubbles were detected within a large velocities range, with 90 % between 4.3 m/s and 28.4 mm/s (Fig. 7(c)).

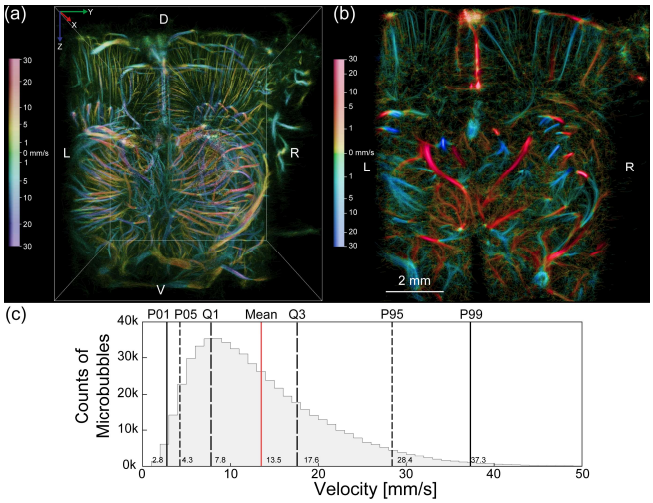

Fig. 7. (a) 3D rendering of the flow velocity with Amira (ThermoFisher) (Power-law compression: 1/3) (b) 600 µm coronal slice at bregma -1.5 mm of the hemodynamic volume up to 30 mm/s. Flows are encoded yellow to red (positive) for upward flows, and green to blue (negative) for downward flows. (c) Histogram of microbubbles' velocities for a total count of 541 k microbubble trajectories.
(Bin width: 1 mm/s, see supplementary video 2).

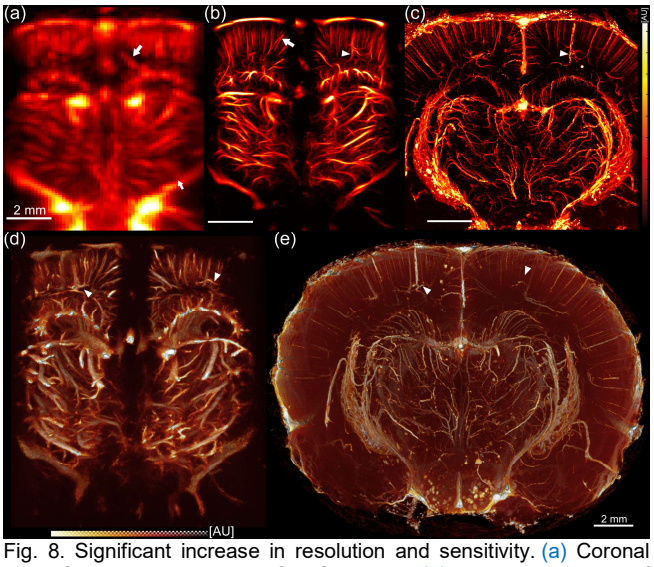

Fig. 8. Significant increase in resolution and sensitivity. (a) Coronal slice of micro Power Doppler CEUS imaging. (b) 2 mm coronal slice of 3D ULM intensity rendering at bregma -2 mm. (c) 2 mm coronal slice of micro-CT with µAngiofil perfusion with MIP rendering. (d) 3D rendering with alpha composition of *in vivo* ULM compared to (e) *ex vivo* micro-CT.
(Power-law compression: 1/2, See supplementary video 3)

D. *Blood vessels detection down to 30 µm diameter*

A significant increase in resolution and sensitivity appears when comparing Contrast-Enhanced Power Doppler in Fig. 8(a) and a 2 mm thick slice of volumetric ULM in Fig. 8(b). Vessels appeared sharper on the ULM slice (white arrows on Fig. 8(a)), and many micro-vessels were revealed (white arrows on Fig. 8(b)).

The *ex vivo* high-resolution micro-CT scan revealed the same vascular architecture with better contrast and sensitivity (Fig. 8(c)). Vessels appeared longer and finer on micro-CT and were not affected by the skull. Some particular vessels could be identified in both ULM and micro-CT but not in PowerDoppler (white triangles). Few vessels were missing on the micro-CT, probably due to a lack of contrast agent perfusion (Fig. 8(d-e)). Only on the ULM images, an unresolved mesh of tracks was present between arterioles and venules and can be associated with the capillary bed. Finally, the brain appeared deformed between *in vivo* transcranial ULM and *ex vivo* micro-CT.

To further characterize this improvement in resolution, a few vessels with different orientations were extracted from the volume and characterized with the diameter and a velocity profile in Fig. 9(a). Vessels could be measured with diameters from 169 µm down to 31 µm. For each vessel, a few trajectories were necessary to ensure a relevant estimation of diameter and velocity. In particular, individual trajectories could not be characterized as vessels. For the selected vessels, the maximal blood velocity was estimated between 6 mm/s up to 44 mm/s. Moreover, FSC provided a maximal consistent spatial frequency of 38 µm with the 2-sigma curve threshold in Fig. 9(b). Features with dimensions smaller than this scale may be confounded with uncorrelated trajectories.

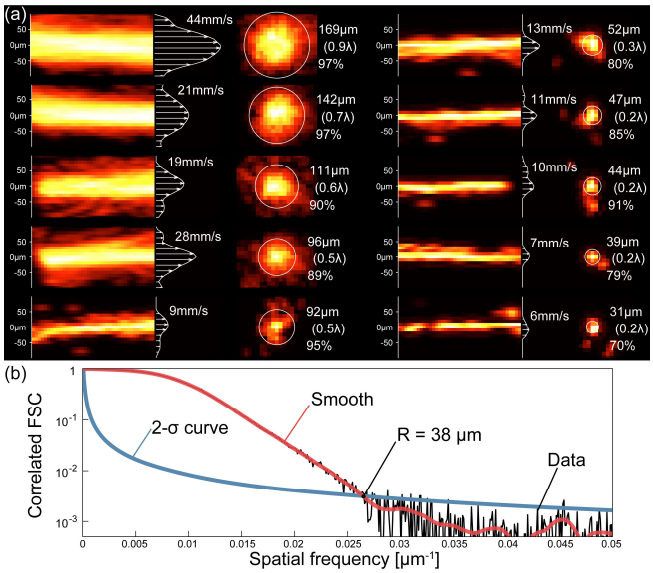

Fig. 9. (a) Manually selected blood vessels with longitudinal and axial intensity projections and main velocity profiles. The percentage represents the ratio of intensity inside the estimated radius, over a disk of 2 radii. (Power-law compression: 1/2) (b) Fourier Shell Correlation computed from two subsets of the list of microbubble trajectories. The intersection with the 2-σ curve gives the maximal consistent spatial frequency.

IV. Discussion

Previous studies demonstrated the ability of 2D ULM to reveal the microvascularization of organs in small animals [10], [13]. However, several issues plague 2D ultrasound imaging and significantly affect ULM. Among others, the velocity estimation of blood flow is poorly estimated because of the elevation projection. In this article, we proposed an implementation of volumetric ULM with a multiplexed matrix probe *in vivo*. Because multiplexing offers different ways of managing apertures in emission and reception, we compared characteristics of three multiplexing combinations with a PSF simulation and *in vitro* with a microbubbles flow in a canal. These tests confirmed the use of the "light" combination, and this was validated *in vivo* in the rat brain with an intact skull with a deep field of view. The imaging sequence and parameters described in the article provided an almost real-time sequence in data saving without the need for a specific ultrasound scanner.

4D systems composed of a high number of channels [27], [30] might be relevant to image fast phenomena such as heart contraction or shear waves (CVR higher than 2 kHz), but ULM does not require extremely high frame rates for blood flow imaging of brain microvascularization. To reduce the channel counts, several teams have been using sparse arrays or row-column approaches [33], [42], but these suffer from degraded PSF and lower SNR. The multiplexed sequence described in this article can be compared to a fully addressed array with multiple synthetic apertures. Both SNR and PSF shapes were preserved but required more transmissions/receptions than a fully addressed array. For blood flow estimation in the rat brain, the limited CVR of 243 Hz allowed flow detection up to 73 mm/s (Fig. 7(c)).

The sensitivity of matrix arrays remains a challenge with respect to the capabilities of linear arrays. At this frequency, transducer elements are wider than the wavelength due to manufacturing limitations, restricting their directivity. Moreover, the element size of the matrix probes is $2 \times 2\ \lambda^2$, which is relatively smaller than the element size of linear arrays. For instance, the elements of an 18 MHz linear probe (L22-14vX, Vermon, Tours, France) are $1 \times 16\ \lambda^2$, benefitting from the focusing lens in elevation. These considerations restrict the sensitivity of matrix arrays and reduce their SNR.

The multiplexing system offers high flexibility management of each switch to create various sub-apertures, including random schemes [32]. We chose to keep the sub-apertures similar to the physical distribution of transducers, i.e. four groups of 32×8 to preserve the emitted pressure field homogenous. As multiplexing requires sub-aperture management, we introduced a new combination of TxAp/RxAp couples offering almost the same imaging capability as the "full" combination but with less transmission: the "light" combination. The "direct" combination studied in our article did not provide a good imaging quality as it suffered from many inhomogeneities (Fig. 4) due to a reduced and heterogenous reception area: a sub-aperture will get more signal if the scatter is facing the center of the reception area. The "light" and "full" combination shared closed results for both *in silico* and *in vitro* experiments with a resolution of 1.5 to 2.0 wavelengths in the *in vivo* range of imaging ([19-78] wavelengths) (Fig. 4). For each emitted plane, the "full" combination requires 6 additional transmissions but with no significant improvements of the imaging quality. Therefore, we used the "light" combination, which allows a higher compounded volume rate of *in vivo* imaging.

Volumetric imaging with a multiplexed probe generates a large quantity of data and can limit long acquisition. Indeed, the sensitivity of ULM imaging to detect small arteries is directly related to the time of acquisition [57]. In comparison, 3D imaging generates 10 times more data than 2D imaging (256 channels with 3 angles versus 1024 channels with 5 plane waves). Our implementation of synthetic summation makes the multiplexing system equivalent to a fully addressed probe in terms of data generation. As we used up to four synthetic emissions for one reception aperture of a plane wave, the synthetic summation reduced the total quantity of data by four without drawbacks.

Transcranial ultrasound imaging affects the signal of scatterers under the skull. The SNR and resolution can be enhanced by increasing the number of plane waves used for volume compounding. However, these extra plane waves generate more data which is problematic for long acquisition. In this study, we reached an SNR of 9 dB for microbubbles under the intact skull with only 5 compounded plane waves. As a comparison, [44] used 12 plane waves with the 4-Aixplorer system in the rat brain with craniectomy and 9 plane waves in [33] with the 2-ULA-OP system for flow canal imaging. This new generation of ultrasound scanners increases the ability of volumetric imaging with fewer plane waves, reducing the data generation and increasing the maximal compounded volume rate. Our implementation enabled 100,000 volumes acquired within 7 min with an SNR suitable for transcranial ULM.

The 3D ULM processing revealed the microvascular system down to almost 30 µm in diameter in the brain. This value was measured on manually selected vessels with enough microbubbles trajectories to get a confident estimation (at least 2 trajectories per voxel). To get a global estimation of the resolution, we used the Fourier Shell Correlation. By exploiting the correlation of spatial frequency, it provided an overall measure, not based on a selected feature of the volume. For the current volume, the 2-sigma threshold [52], [54], [55] gave a resolution of 38 µm, slightly higher than the segmented vessels. This value could be improved by extending the acquisition time. However, the maximal resolution is also limited by the localization precision, degraded by the aberration of the skull. In addition, a disorganized and sparse mesh of isolated microbubble trajectories appeared between resolved vessels (Fig. 8). We suggest it reflects the vascularization at a smaller scale than the localization precision, such as capillaries. Further local averaging could bring an estimation of flux or a dynamic of perfusion.

The high-resolution micro-CT scan confirms the angiography provided with ULM without hemodynamic information. Both imaging techniques show the same vascular system down to arterioles and venules. The brain morphology appears modified in micro-CT scan with tissue expansion and shrinkage due to brain fixation and extraction. Micro-CT provides a more contrasted and resolved imaging thanks to µAngiofil perfusion coupled with an extended exposure scan (>8h), but few vessels can be missing if the perfusion is not total. Micro-CT is still a reference for high-resolution angiography but not suitable for non-invasive imaging nor hemodynamic angiography.

We selected a 7.8 MHz frequency as a trade-off between resolution and penetration and also the field-of-view. At higher frequencies, the absorption of the skull degrades the imaging system [58]. The field of view must be considered when selecting the frequency. In our system, the element's pitch was 2 wavelengths, and the 32 elements in the lateral direction were adapted for brain imaging of small animals. A higher frequency involves a reduced field of view or larger elements with a detrimental directivity of transducers. Lower frequencies could improve the penetration through the skull but would reduce the localization precision. Besides, bigger voxels tend to host more microbubbles and increase PSF overlapping, constraining the microbubbles' injection rate.

The volumetric field-of-view provided by this matrix array alleviated the plane selection of plane imaging, highly user-dependent in ultrasound imaging. Indeed, minimal probe alignment was necessary, and no motor was included in the system since a large volume of the brain could be observed under the probe. 3D ULM also eliminated the pre-selection of the imaging plane. Exploration of the various imaging sections could be done in post-treatment upon the entire dataset.

The association of microbubble trajectories and timestamps yielded a range of velocity of [4.3-28.4 mm/s] (for 90 % of the microbubbles). This scale was narrower than the range provided by the tracking algorithm [0-73 mm/s]. The lack of low-velocity [9], [59] can be explained by the SVD filtering that removed slowly moving signals. Lower velocity microbubbles could be enhanced with non-linear imaging methods [16], [60]. Higher velocities were excluded due to the lack of appropriate microbubble pairing.

The processing time of 3D ULM is still binding for routine usage with large cohorts of animals or patients. The current implementation with CUDA-based beamforming, non-interpolated localization scheme, and asynchronous processing reduced the processing time to 3 hours for 100,000 volumes. In addition, reducing the number of volumes to 33,000 can already provide a draft of the vascularization, reducing acquisition time, data size, and processing time. Real-time imaging remains a future endeavor, and actual processing times should be compared to those required by common imaging techniques, such as MRI or scanner (<1 hour).

A drawback of the implementation of volumetric imaging with a MUX system is the reduced compounded volume rate. The numerous TxAp/RxAp couples imposed by the multiplexed probe limited the CVR of imaging at 243 Hz for 15 mm imaging depth but was sufficient to track microbubbles up to 73 mm/s. The "direct" combination could provide a higher volume rate but with heterogenous localizations (Fig. 5). The main limit of a reduced volume rate arises for motion correction for rapid displacements [61]. In our experiments, the rat's head was constrained in a stereotaxic frame to prevent most head motion and did not require motion correction. However, organs such as the kidney, liver, or heart are more impacted by breathing or heartbeat and require motion correction algorithms. Furthermore, the transfer of this approach to human imaging may be more subjected to motion because the head cannot be restrained as in a stereotaxic frame, particularly in ambulatory conditions or injured patients.

The attenuation and aberration of the skull degraded the image quality in a few regions of our acquisitions (Fig. 6), mainly under complex structures such as ridges and sutures. Attenuation could be compensated with a higher-pressure field, or by increasing the number of compounded plane waves. For the same compounded volume rate, our implementation did not tolerate additional plane waves. Due to the higher speed of sound in the bone, phase aberrations appear in the RF data and degrade the beamforming process. [62] proposed a phase aberration correction to adjust delays in the beamforming process. It seems efficient for phantom imaging of a canal but requires many adaptations for volumetric imaging under the rat brain. A precise characterization of the aberration law behind each transducer would have to be obtained by measuring the phase shift between microbubbles signals and a theoretical time-of-flight hyperbola. However, the wide elements may miss an accurate aberration law by averaging the skull thickness variation over about two wavelengths, providing a suboptimal sampling of the aberration law. Finally, in post-processing, multiple isoplanatic patches would be required to resolve the aberration in any part of the field-of-view, with an additional complexity brought by volumetric imaging. It may reduce the shadow effect and increase the localization precision. To overcome this limitation, we decided to tilt the probe to focus on hidden zones exploiting the thin parietal bone window.

However, the translation to human imaging will require solving these limitations of transcranial imaging to reach an accurate microvascular mapping. For instance, emitted acoustic pressures should be adapted to the specific attenuation of each patient's skull to attain an appropriate SNR inside the skull and avoid microbubbles destruction inside the brain. Moreover, regions shadowed by local spikes in skull attenuation could lead to misinterpretation in blood perfusion. The interpretation of ULM images must consider this lack of information and avoid any conclusions in these areas. For example, in [23], the microvascularization appeared resolved and enhanced only within the field-of-view of the phased-array probe, which impacted clinical evaluation. A better knowledge of skull attenuation may widen the regions of interest where microvascularization can be characterized.

This study described 3D imaging of microvascularization with a multiplexed ultrasound scanner. ULM becomes highly beneficial when implemented in 3-dimensions as it corrects planar projection, motion, and user dependency. In particular, it avoids any bias due to plane selection during the experiment as the analysis is performed over the entire volumetric dataset. Because of its relative simplicity, this multiplexed portable system can be easily implemented in most animal imaging platforms. It improves upon other imaging modalities also impacted by depth, resolution, or incompatibilities with *in vivo* physiological measurements. The quasi-isotropic sensitivity and resolution of the probe highlighted the brain's complex vascularization and would be interesting in other vital organs such as the kidney and heart. In neurology, it would provide a valuable tool for describing the interaction between microvascularization and brain function. Various disease processes implicating arterioles and venules, such as cancer or diabetes, could be better described *in vivo* and studied at an early stage. It also opens the possibility for human diagnosis of microvascular diseases as it alleviates both the conventional resolution limit of ultrasound and its conventional planar implementation with a compact scanner.

V. Conclusion

ULM reveals the microvascular system of organs in alive animals. Recent developments on ultrasound scanners and probes have permitted its extension to volumetric imaging. We demonstrated 3D transcranial ULM with a research-grade ultrasound scanner in the rat brain with an intact skull, highlighting a complex vascular and hemodynamic organization down to arterioles and venules. 3D ULM could bring promising features for the understanding and diagnostics of organs and their diseases.

VI. Acknowledgments

We would like to Ruslan Hlushchuk for his valuable advice on the perfusion of µAngiofil and micro-CT scanning parameters. We also thank Dr. Christine Chappard and IMOSAR facility (Université Paris Diderot, INSERM, CNRS) for its expertise and access to micro-computed tomography.

VII. References

[1] C. S. Roy and C. S. Sherrington, "On the Regulation of the Blood-supply of the Brain," The Journal of Physiology, vol. 11, no. 1–2, pp. 85–158, 1890, doi: 10.1113/jphysiol.1890.sp000321.

[2] R. Hlushchuk et al., "Innovative high-resolution microCT imaging of animal brain vasculature," Brain Struct Funct, vol. 225, no. 9, pp. 2885–2895, Dec. 2020, doi: 10.1007/s00429-020-02158-8.

[3] S. M. Jorgensen et al., "Three-dimensional imaging of vasculature and parenchyma in intact rodent organs with X-ray micro-CT," American Journal of Physiology-Heart and Circulatory Physiology, vol. 275, no. 3, pp. H1103–H1114, Sep. 1998, doi: 10.1152/ajpheart.1998.275.3.H1103.

[4] A. Ertürk et al., "Three-dimensional imaging of solvent-cleared organs using 3DISCO," Nat Protoc, vol. 7, no. 11, pp. 1983–1995, Nov. 2012, doi: 10.1038/nprot.2012.119.
[5] N. Renier et al., "iDISCO: A Simple, Rapid Method to Immunolabel Large Tissue Samples for Volume Imaging," Cell, vol. 159, no. 4, pp. 896–910, Nov. 2014, doi: 10.1016/j.cell.2014.10.010.
[6] K. Chung and K. Deisseroth, "CLARITY for mapping the nervous system," Nat Methods, vol. 10, no. 6, pp. 508–513, Jun. 2013, doi: 10.1038/nmeth.2481.
[7] R. Tomer et al., "Advanced CLARITY for rapid and high-resolution imaging of intact tissues," Nat Protoc, vol. 9, no. 7, pp. 1682–1697, Jul. 2014, doi: 10.1038/nprot.2014.123.
[8] E. A. Susaki et al., "Whole-Brain Imaging with Single-Cell Resolution Using Chemical Cocktails and Computational Analysis," Cell, vol. 157, no. 3, pp. 726–739, Apr. 2014, doi: 10.1016/j.cell.2014.03.042.
[9] A. Y. Shih, "Two-Photon Microscopy as a Tool to Study Blood Flow and Neurovascular Coupling in the Rodent Brain," p. 33, 2012, doi: 10.1038/jcbfm.2011.196.
[10] K. Christensen-Jeffries et al., "Super-resolution Ultrasound Imaging," Ultrasound in Medicine & Biology, vol. 46, no. 4, pp. 865–891, Apr. 2020, doi: 10.1016/j.ultrasmedbio.2019.11.013.
[11] O. Couture et al., "Microbubble ultrasound super-localization imaging (MUSLI)," in Ultrasonics Symposium (IUS), 2011 IEEE International, 2011, pp. 1285–1287. doi: 10.1109/ULTSYM.2011.6293576.
[12] O. Couture et al., "Ultrasound Localization Microscopy and Super-Resolution: A State of the Art," IEEE Trans. Ultrason., Ferroelect., Freq. Contr., vol. 65, no. 8, pp. 1304–1320, Aug. 2018, doi: 10.1109/TUFFC.2018.2850811.
[13] C. Errico et al., "Ultrafast ultrasound localization microscopy for deep super-resolution vascular imaging," Nature, vol. 527, no. 7579, pp. 499–502, Nov. 2015, doi: 10.1038/nature16066.
[14] L. Milecki et al., "A Deep Learning Framework for Spatiotemporal Ultrasound Localization Microscopy," IEEE Trans. Med. Imaging, pp. 1–1, 2021, doi: 10.1109/TMI.2021.3056951.
[15] K. Christensen-Jeffries et al., "In Vivo Acoustic Super-Resolution and Super-Resolved Velocity Mapping Using Microbubbles," IEEE Transactions on Medical Imaging, vol. 34, no. 2, pp. 433–440, Feb. 2015, doi: 10.1109/TMI.2014.2359650.
[16] J. Foiret et al., "Ultrasound localization microscopy to image and assess microvasculature in a rat kidney," Scientific Reports, vol. 7, no. 1, p. 13662, Dec. 2017, doi: 10.1038/s41598-017-13676-7.
[17] P. Song et al., "Improved Super-Resolution Ultrasound Microvessel Imaging with Spatiotemporal Nonlocal Means Filtering and Bipartite Graph-Based Microbubble Tracking," IEEE Trans Ultrason Ferroelectr Freq Control, vol. 65, no. 2, pp. 149–167, Feb. 2018, doi: 10.1109/TUFFC.2017.2778941.
[18] C. Huang et al., "Short Acquisition Time Super-Resolution Ultrasound Microvessel Imaging via Microbubble Separation," Sci Rep, vol. 10, no. 1, p. 6007, Dec. 2020, doi: 10.1038/s41598-020-62898-9.
[19] F. Lin et al., "3-D Ultrasound Localization Microscopy for Identifying Microvascular Morphology Features of Tumor Angiogenesis at a Resolution Beyond the Diffraction Limit of Conventional Ultrasound," Theranostics, vol. 7, no. 1, pp. 196–204, Jan. 2017, doi: 10.7150/thno.16899.
[20] M. R. Lowerison et al., "Ultrasound localization microscopy of renal tumor xenografts in chicken embryo is correlated to hypoxia," Scientific Reports, vol. 10, no. 1, Art. no. 1, Feb. 2020, doi: 10.1038/s41598-020-59338-z.
[21] W. Zhang et al., "Super-Resolution Ultrasound Localization Microscopy on a Rabbit Liver VX2 Tumor Model: An Initial Feasibility Study," Ultrasound in Medicine & Biology, May 2021, doi: 10.1016/j.ultrasmedbio.2021.04.012.
[22] J. Zhu et al., "3D Super-Resolution US Imaging of Rabbit Lymph Node Vasculature in Vivo by Using Microbubbles," Radiology, vol. 291, no. 3, pp. 642–650, Jun. 2019, doi: 10.1148/radiol.2019182593.
[23] C. Demené et al., "Transcranial ultrafast ultrasound localization microscopy of brain vasculature in patients," Nat Biomed Eng, vol. 5, no. 3, Art. no. 3, Mar. 2021, doi: 10.1038/s41551-021-00697-x.
[24] C. Huang et al., "Super-resolution ultrasound localization microscopy based on a high frame-rate clinical ultrasound scanner: an in-human feasibility study," Phys. Med. Biol., vol. 66, no. 8, p. 08NT01, Apr. 2021, doi: 10.1088/1361-6560/abef45.
[25] G. Montaldo et al., "Coherent plane-wave compounding for very high frame rate ultrasonography and transient elastography," IEEE Transactions on Ultrasonics, Ferroelectrics and Frequency Control, vol. 56, no. 3, pp. 489–506, Mar. 2009, doi: 10.1109/TUFFC.2009.1067.
[26] M. Tanter and M. Fink, "Ultrafast imaging in biomedical ultrasound," IEEE Transactions on Ultrasonics, Ferroelectrics, and Frequency Control, vol. 61, no. 1, pp. 102–119, Jan. 2014, doi: 10.1109/TUFFC.2014.2882.
[27] J. A. Jensen et al., "SARUS: A synthetic aperture real-time ultrasound system," IEEE Trans. Ultrason., Ferroelect., Freq. Contr., vol. 60, no. 9, pp. 1838–1852, Sep. 2013, doi: 10.1109/TUFFC.2013.2770.
[28] M. Correia et al., "3D elastic tensor imaging in weakly transversely isotropic soft tissues," Phys. Med. Biol., vol. 63, no. 15, p. 155005, Jul. 2018, doi: 10.1088/1361-6560/aacfaf.
[29] L. Petrusca et al., "Fast Volumetric Ultrasound B-Mode and Doppler Imaging with a New High-Channels Density Platform for Advanced 4D Cardiac Imaging/Therapy," Applied Sciences, vol. 8, no. 2, p. 200, Jan. 2018, doi: 10.3390/app8020200.
[30] J. Provost et al., "3D ultrafast ultrasound imaging in vivo," Physics in Medicine and Biology, vol. 59, no. 19, pp. L1–L13, Oct. 2014, doi: 10.1088/0031-9155/59/19/L1.
[31] C. Rabut et al., "4D functional ultrasound imaging of whole-brain activity in rodents," Nat Methods, vol. 16, no. 10, pp. 994–997, Oct. 2019, doi: 10.1038/s41592-019-0572-y.
[32] M. Bernal et al., "High-frame-rate volume imaging using sparse-random-aperture compounding," Phys. Med. Biol., vol. 65, no. 17, p. 175002, Sep. 2020, doi: 10.1088/1361-6560/ab9372.
[33] S. Harput et al., "3-D Super-Resolution Ultrasound Imaging With a 2-D Sparse Array," IEEE Transactions on Ultrasonics, Ferroelectrics, and Frequency Control, vol. 67, no. 2, pp. 269–277, Feb. 2020, doi: 10.1109/TUFFC.2019.2943646.
[34] E. Roux et al., "Experimental 3-D Ultrasound Imaging with 2-D Sparse Arrays using Focused and Diverging Waves," Scientific Reports, vol. 8, no. 1, Dec. 2018, doi: 10.1038/s41598-018-27490-2.
[35] T. L. Christiansen et al., "3-D imaging using row–column-addressed arrays with integrated apodization— part ii: transducer fabrication and experimental results," IEEE Trans. Ultrason., Ferroelect., Freq. Contr., vol. 62, no. 5, pp. 959–971, May 2015, doi: 10.1109/TUFFC.2014.006819.
[36] M. F. Rasmussen et al., "3-D imaging using row-column-addressed arrays with integrated apodization - part i: apodization design and line element beamforming," IEEE Trans. Ultrason., Ferroelect., Freq. Contr., vol. 62, no. 5, pp. 947–958, May 2015, doi: 10.1109/TUFFC.2014.006531.
[37] J. Sauvage et al., "4D Functional Imaging of the Rat Brain Using a Large Aperture Row-Column Array," IEEE Transactions on Medical Imaging, vol. 39, no. 6, pp. 1884–1893, Jun. 2020, doi: 10.1109/TMI.2019.2959833.
[38] C. Brunner et al., "A Platform for Brain-wide Volumetric Functional Ultrasound Imaging and Analysis of Circuit Dynamics in Awake Mice," Neuron, vol. 108, no. 5, pp. 861-875.e7, Dec. 2020, doi: 10.1016/j.neuron.2020.09.020.
[39] J. Yu et al., "Design of a Volumetric Imaging Sequence Using a Vantage-256 Ultrasound Research Platform Multiplexed With a 1024-Element Fully Sampled Matrix Array," IEEE Trans. Ultrason., Ferroelect., Freq. Contr., vol. 67, no. 2, pp. 248–257, Feb. 2020, doi: 10.1109/TUFFC.2019.2942557.
[40] Y. Desailly et al., "Sono-activated ultrasound localization microscopy," Applied Physics Letters, vol. 103, no. 17, p. 174107, Oct. 2013, doi: 10.1063/1.4826597.
[41] M. A. O'Reilly and K. Hynynen, "A super-resolution ultrasound method for brain vascular mapping," Med Phys, vol. 40, no. 11, Nov. 2013, doi: 10.1118/1.4823762.
[42] J. A. Jensen et al., "Three-Dimensional Super-Resolution Imaging Using a Row–Column Array," IEEE Trans. Ultrason., Ferroelect., Freq. Contr., vol. 67, no. 3, pp. 538–546, Mar. 2020, doi: 10.1109/TUFFC.2019.2948563.
[43] B. Heiles et al., "Ultrafast 3D Ultrasound Localization Microscopy Using a 32x32 Matrix Array," IEEE Trans. Med. Imaging, vol. 38, no. 9, pp. 2005–2015, Sep. 2019, doi: 10.1109/TMI.2018.2890358.
[44] B. Heiles et al., "Volumetric ultrasound localization microscopy of the whole brain microvasculature," Sep. 2021. doi: 10.1101/2021.09.17.460797.
[45] M. Schneider, "Characteristics of SonoVueTM," Echocardiography, vol. 16, no. s1, pp. 743–746, Oct. 1999, doi: 10.1111/j.1540-8175.1999.tb00144.x.
[46] C. Demene et al., "Spatiotemporal Clutter Filtering of Ultrafast Ultrasound Data Highly Increases Doppler and fUltrasound Sensitivity," IEEE Transactions on Medical Imaging, vol. 34, no. 11, pp. 2271–2285, Nov. 2015, doi: 10.1109/TMI.2015.2428634.
[47] Y. Desailly et al., "Contrast enhanced ultrasound by real-time spatiotemporal filtering of ultrafast images," Physics in Medicine and Biology, vol. 62, no. 1, pp. 31–42, Jan. 2017, doi: 10.1088/1361-6560/62/1/31.
[48] A. Yu and L. Lovstakken, "Eigen-based clutter filter design for ultrasound color flow imaging: a review," IEEE Trans. Ultrason., Ferroelect.,

Freq. Contr., vol. 57, no. 5, pp. 1096–1111, May 2010, doi: 10.1109/TUFFC.2010.1521.
[49] B. Heiles, "3D Ultrasound Localization Microscopy," Ph.D. dissertation, PSL Research University, Paris, France, 2019. Accessed: Sep. 30, 2020. [Online]. Available: https://tel.archives-ouvertes.fr/tel-02478291
[50] B. Heiles et al., "Performance benchmarking of microbubble-localization algorithms for ultrasound localization microscopy," Nature Biomedical Engineering, 2021, In press.
[51] R. Parthasarathy, "Rapid, accurate particle tracking by calculation of radial symmetry centers," Nat Methods, vol. 9, no. 7, pp. 724–726, Jul. 2012, doi: 10.1038/nmeth.2071.
[52] V. Hingot et al., "Measuring Image Resolution in Ultrasound Localization Microscopy," IEEE Transactions on Medical Imaging, vol. 40, no. 12, pp. 3812–3819, Dec. 2021, doi: 10.1109/TMI.2021.3097150.
[53] R. P. J. Nieuwenhuizen et al., "Measuring image resolution in optical nanoscopy," Nat Methods, vol. 10, no. 6, pp. 557–562, Jun. 2013, doi: 10.1038/nmeth.2448.
[54] N. Banterle et al., "Fourier ring correlation as a resolution criterion for super-resolution microscopy," Journal of Structural Biology, vol. 183, no. 3, pp. 363–367, Sep. 2013, doi: 10.1016/j.jsb.2013.05.004.
[55] M. van Heel and M. Schatz, "Fourier shell correlation threshold criteria," Journal of Structural Biology, vol. 151, no. 3, pp. 250–262, Sep. 2005, doi: 10.1016/j.jsb.2005.05.009.
[56] E. A. Papp et al., "Waxholm Space atlas of the Sprague Dawley rat brain," NeuroImage, vol. 97, pp. 374–386, Aug. 2014, doi: 10.1016/j.neuroimage.2014.04.001.
[57] V. Hingot et al., "Microvascular flow dictates the compromise between spatial resolution and acquisition time in Ultrasound Localization Microscopy," Sci Rep, vol. 9, no. 1, p. 2456, Dec. 2019, doi: 10.1038/s41598-018-38349-x.
[58] G. Pinton et al., "Attenuation, scattering, and absorption of ultrasound in the skull bone: Absorption of ultrasound in the skull bone," Medical Physics, vol. 39, no. 1, pp. 299–307, Dec. 2011, doi: 10.1118/1.3668316.
[59] C. B. Schaffer et al., "Two-Photon Imaging of Cortical Surface Microvessels Reveals a Robust Redistribution in Blood Flow after Vascular Occlusion," PLoS Biol, vol. 4, no. 2, p. e22, Jan. 2006, doi: 10.1371/journal.pbio.0040022.
[60] D. H. Simpson and P. N. Burns, "Pulse inversion Doppler: a new method for detecting nonlinear echoes from microbubble contrast agents," in 1997 IEEE Ultrasonics Symposium Proceedings. An International Symposium (Cat. No.97CH36118), Toronto, Ont., Canada, 1997, vol. 2, pp. 1597–1600. doi: 10.1109/ULTSYM.1997.663301.
[61] V. Hingot et al., "Subwavelength motion-correction for ultrafast ultrasound localization microscopy," Ultrasonics, vol. 77, pp. 17–21, May 2017, doi: 10.1016/j.ultras.2017.01.008.
[62] D. E. Soulioti et al., "Super-Resolution Imaging Through the Human Skull," IEEE Trans. Ultrason., Ferroelect., Freq. Contr., vol. 67, no. 1, pp. 25–36, Jan. 2020, doi: 10.1109/TUFFC.2019.2937733.